Shining light on interstellar matter : a laboratory study

Paardekooper, D.M.

4

METHANE ICE PHOTOCHEMISTRY AND KINETIC STUDY USING LASER DESORPTION TIME-OF-FLIGHT MASS SPECTROMETRY AT 20 K

The ice photochemistry of pure methane (CH_4) is studied at 20 K upon VUV irradiation from a microwave discharge H_2 flow lamp. Laser Desorption Post-Ionization Time-Of-Flight Mass Spectrometry (LDPI TOF-MS) is used for the first time to determine branching ratios of primary reactions leading to CH_3, CH_2, and CH radicals, typically for fluences as expected in space. This study is based on a stable end-products analysis and the mass spectra are interpreted using an appropriate set of coupled reactions and rate constants. This yields clearly different values from previous gas phase studies. The matrix environment as well as the higher efficiency of reverse reactions in the ice clearly favor CH_3 radical formation as the main first generation photoproduct.

J.-B. Bossa, D. M. Paardekooper, K. Isokoski, and H. Linnartz, *Methane ice photochemistry and kinetic study using laser desorption time-of-flight mass spectrometry at 20 K*, Phys. Chem. Chem. Phys., 17, (2015) 17346.

4.1 INTRODUCTION

At the present time, more than 180 different species not including isotopologues have been observed in interstellar and circumstellar media. Models of interstellar chemistry involving both gas-phase and solid-phase reactions are employed to understand the complex chemical formation route of the observed species and to predict their abundances in the regions where they reside (van Dishoeck, 2014). The reliability of these models depends on the accuracy of the reaction rate coefficients that are contained in databases for use in astrochemistry; e.g., UMIST Database for Astrochemistry (McElroy et al., 2013), NIST Chemical Kinetics Database (Manion et al., Release 1.6.8, Data version 2013.03, National Institute of Standards and Technology, Gaithersburg, Mary- land, 20899-8320, 2013, http://kinetics.nist.gov/), KInetic Database for Astrochemistry (Wakelam et al., 2012). For the gas phase, accurate data have been derived in the laboratory, but in the solid phase such data are still largely lacking (Wakelam et al., 2010). Moreover, processes on icy grains cannot be considered to be isolated processes. Nevertheless, it is a long-standing problem that in the absence of experimental data on ice films, astrochemical models use gas phase reaction rate coefficients instead, which are often extrapolated beyond measured temperatures, to determine the abundance of reactants and products in interstellar ices during the different stages of star formation. This may lead to considerable errors.

A few laboratory studies have been reported that mention branching ratio estimations for photochemical experiments simulating UV fluences as expected for typical dense cloud lifetimes (Gerakines et al., 1996; Öberg et al., 2009). For some pure ices, backward reactions that convert products to the initial reactant are so fast that forward reactions cannot be investigated directly. For example, the solid-state methylamine (CH_3NH_2) photodissociation pathways have been unraveled by using carbon monoxide (CO) as an H atom scavenger (Bossa et al., 2012a). Genuine kinetic studies involving energetic processing of ices are difficult to perform and need accurate and time resolved surface science techniques. The extensive and systematic study of thermal reactivity in binary and ternary ice mixtures together with diffusion measurements have already provided kinetic parameters (Theulé et al. (2013); Mispelaer et al. (2013) and references therein). Hydrogen – deuterium substitution experiments on pure methylamine ice (Oba et al., 2014) and energetic electron irradiations on a pure methane (CH_4) ice (Bennett et al., 2006) and on a NH_3:CH_4 binary ice mixture (Kim & Kaiser, 2011) have been kinetically investigated by combining reflection absorption infrared spectroscopy (RAIRS) and mass spectrometry during temperature programmed desorption experiments (TPD). In these latter studies, the quantitative analysis relies on the column densities of both reactants and products as a function of the different energetic processing times. These values are generally determined from the mid-infrared spectra by integrating – preferably – non-overlapping vibrational bands and by using the corresponding band strengths from the literature, i.e., the A-values written in cm molecule^{-1} unit. Overlapping infrared features are common when working with complex ices, i.e., composed by more than three different constituents. Band strengths and infrared band profiles are known to be strongly dependent on the ice temperature and on the ice composition (Öberg et al., 2007), thus larger uncertainties may arise when more complex species form in the ice. Intermediate species like radicals are also difficult to observe in the solid phase even when trapped at cryogenic temperatures. Only few of them are stable and can be directly observed in the mid-infrared (e.g., HCO or CH_3) (Gerakines et al., 1996; Bennett et al., 2006). Electron Paramagnetic Resonance (EPR) implemented for cryogenic materials (Toriyama & Iwasaki, 1979; Shkrob et al., 2011) should be ideal to monitor radicals during an irradiation, but this technique has, to our knowledge, not often been used in the field of laboratory astrophysics (Zhitnikov & Dmitriev, 2002). Another

suitable experimental technique that may compensates the current limitations of regular surface science techniques (e.g., RAIRS and TPD) is the Laser Desorption Post-Ionization Time-Of-Flight Mass Spectrometry (LDPI TOF-MS) (Focsa & Destombes, 2001; Gudipati & Yang, 2012). This technique allows the *in situ* analysis of small fractions of a processed ice sample at different irradiation times, thus allowing kinetic studies, as demonstrated in a recent technical review (Paardekooper et al., 2014).

The focus here is on solid methane (CH_4). Interstellar methane (CH_4) is ubiquitous and the solid phase abundances range from 1 to 5 % relative to H_2O, depending on the targeted source type (Gibb et al., 2004; Öberg et al., 2011). Gas phase methane (CH_4) photolysis is the main source of more complex hydrocarbons in the atmospheres of Titan (Wilson & Atreya, 2000; Romanzin et al., 2005) and the giant planets (Dobrijevic et al., 2003; Smith & Nash, 2006). Several reviews dedicated to the different photolysis pathways of gas phase methane in the Lyman-α wavelength region demonstrate the complex photochemistry and list contradictory results concerning the branching ratios between the various products (see Romanzin et al., 2005; Blitz & Seakins, 2012, and references therein). These differences were explained by the collisional conditions and the nature of the probed processes (Romanzin et al., 2005). In contrast to a gas phase environment, solid materials present higher densities and reduced mobilities of their constituents. Thus atoms and radicals trapped within a processed cold ice can efficiently recombine and reform the initial material. Therefore, backward reactions slow down the primary photodissociation processes and one can expect a drastically different chemical evolution scenario compared to the one observed in the gas phase studies (Okabe, 1978; Yung & Demore, 1999).

The objective of this present kinetic study is to understand – in a bottom-up approach and using the LDPI TOF-MS technique – the methane photochemistry at cryogenic temperatures and therefore in the solid phase, and to provide for the first time effective rate coefficients and branching ratios for primary processes at 20 K.

4.2 EXPERIMENTAL APPROACH

The experiments were carried out in the novel, contamination-free ultra-high vacuum (UHV) setup MATRI^{2}CES, thoroughly described in Paardekooper et al. (2014). The central unit is an UHV chamber in which thin ice samples can be grown with monolayer precision onto an off-centred gold-coated copper cylinder ending in a rectangular flat sampling edge surface. The substrate holder is mounted on a closed-cycle helium cryostat that, in conjunction with resistive heating, allows for temperature control from 20 to 300 K with a relative precision of 0.1 K (Lakeshore model 331). Only gas phase methane (CH_4, Praxair, purity 99.9995 %) is introduced into the main chamber with an aperture adjusted leak valve following a front deposition procedure. During deposition at 20 K, the substrate holder is continuously (vertically) translating back and forth to achieve a relatively flat ice growth (similar as the spray painting technique). The thickness of the ice samples is typically around 50 ML. The thickness is determined in separate experiments but with identical deposition procedures and using laser optical interference (Bossa et al., 2012b) ($\lambda = 632.8$ nm, He-Ne laser, Thorlabs HRS015) with a refractive index of 1.329 (Brunetto et al., 2008). The vacuum ultraviolet (VUV) irradiation ($\lambda > 120$ nm) is generated by a microwave discharge H_2 flow lamp (Opthos instruments) separated from the main UHV chamber by a UHV magnesium fluoride (MgF_2) window with a cut-off wavelength at 120 nm. Lamp settings during irradiation are $P_{H_2} = 7 \times 10^{-1}$ mbar, F-type quartz-lamp geometry, microwave forward power 80 %, and reflected power of 10 %. The integrated emission flux of the microwave-discharge H_2 lamp in the 120 – 200 nm wavelength range at 140 mm (from the lamp window to the sample) is $2-4 \times 10^{13}$ photons s^{-1} cm^{-2}. The spectral profile of the lamp mainly contains Lyman-α ($\lambda = 121.6$ nm) photons emitted

(~ 75%) together with the remaining $\lambda = 160$ nm photons (see Chen et al., 2014; Ligterink et al., 2015, Chapter 3). The substrate holder is directly connected to a two axis translation stage system: horizontal (y) and vertical (z) motions are allowed in order to always expose non-overlapping *fresh spots* of an ice sample to the laser desorption beam for kinetic study and for mass spectra averaging. The VUV emission is stopped, before ice diagnostics, for positioning the substrate holder at the right (y, z) coordinate. Meanwhile, we expect that radical diffusion and reactivity are efficient enough even at 20 K, especially for the methyl radical for which the diffusion is already efficient even diluted in water (Öberg et al., 2010). We assume that no reactions (i.e., upon diffusion and recombination) occurs during the laser ablation process and that the observed products are representative of the ice photochemistry prior to ablation. Partial ablations of hydrocarbon-rich cryogenic ices are achieved using the unfocused ~ 1.25 mm diameter) third harmonic beam of a Nd:YAG laser (Polaris II, New Wave Research, 355 nm, 10 Hz repetition rate, 143 mJ cm^{-2} energy density without attenuation, unpolarized). Laser desorption is used to bring species into the gas phase, generally as a desorption plume. Laser attenuation, resulting in a laser pulse energy of 8-9 mJ cm^{-2} and ion extraction time are optimised to probe the desorption plume where both clustering and chemical reactions are negligible upon desorption compared to the VUV irradiation effects. The local temperature rise where the laser hits the ice/gold interface is estimated around 600 K (El-Adawi & Elshehawey, 1986) (upper limit obtained without laser attenuation) after a 4 ns laser pulse striking the vacuum/ice/gold three-phase layered structure (Dohnálek et al., 2003; Bossa et al., 2014) at an incident angle of 30°, with a reflectivity $(R_s + R_p)/2 = 0.39$. Typically around 220 laser ablation pulses are needed to record one averaged time-of-flight spectrum with good signal-to-noise ratio. Ablated ice constituents are subsequently ionised by an orthogonal beam of electrons generated by a 70 eV electron impact ion source located underneath the UHV chamber, hence allowing laser-desorption and ionisation events occurring at the same spot. Positive ions are generated between the extraction and repeller plates of the time-of-flight system (Jordan TOF Products, Inc.) for an optimum ion transmission. After electron impact ionisation, cations with different masses are accelerated into a second UHV time-of-flight chamber/tube in reflection mode for mass-separation following the different arrival times to the 40 mm MCP detector. A 3-point internal calibration is then performed for each averaged spectrum using fragment ion peaks and/or the molecular ion peak of the initial ice material.

4.3 RESULTS

The electronic absorption spectrum of gas phase CH_4 begins for wavelengths below 140 nm (Lee & Chiang, 1983). The solid phase CH_4 absorption spectra slightly shift to shorter wavelengths compared to the gas phase (Cruz-Diaz et al., 2014), and present three non resolved absorptions near Lyman-α. Therefore, the Lyman-α photons emitted from the microwave-discharge H_2 flow lamp (and not the 160 nm photons) likely correspond to the main incident radiation susceptible to be absorbed by the pure CH_4 ice. Among the different photodissociation channels accessible near Lyman-α, three fragments (CH_3, CH_2, and CH radicals) can form stable end-products like C_2H_6, C_2H_4, and C_2H_2 hydrocarbons. The branching ratios of the solid state photodissociation pathways leading to these radicals, therefore, can be determined by monitoring the molar fractions of the three stable photoproducts together with the decrease of methane as a function of irradiation time. In the following, specific attention will be paid to hydrocarbons up to two carbon atoms only, i.e., four molecules in total namely methane, ethane, ethylene, and acetylene. Note that the different possible electronic states (singlet and triplet) of CH_2 are not distinguished in this study.

In the following the results are presented. We employed highly sensitive laser desorption post ionisation time-of-flight mass spectrometry to identify the molecular complexity emerging during the VUV irradiation of a pure CH_4 ice at 20 K. At different predefined irradiation times, i.e., 2, 4, 8, 12, 16, 24, 32, 40, 48, 56, 64, 72, 80, 88, and 96 min. (the last value corresponding to maximum 10^7 years of photolysis in dense molecular clouds), the VUV lamp is switched off and a mass spectrum is recorded. Since we are limited to nine measurements per processed ice, experiments are repeated up to four times with overlapping irradiation times as repeatability check points.

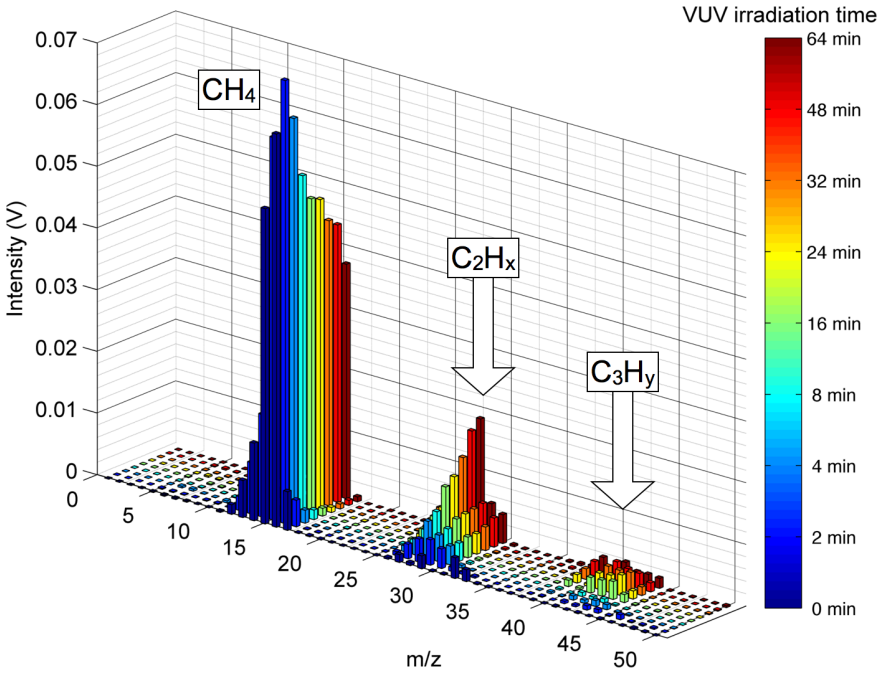

Figure 4.1: ReTOF 70 eV electron impact mass spectra sample as a function of the VUV irradiation time (color bar) of the initial (CH_4) and newly formed ice products (C_2H_x and C_3H_y), with x = 2,4,6 and y = 4,6,8.

Figure 4.1 shows a typical example of ReTOF mass spectra as a function of irradiation time (2, 4, 8, 16, 24, 32, 48, and 64 min.), with 0 min. the reference mass spectrum recorded right before starting the photolysis. The spectra display the signal intensity in Volt as a function of m/z ratios. The intensity can be directly correlated to the total counts of the ionised species coming from the laser desorption process that induces desorption of the ice constituents at well-defined irradiation time and processed ice spots. For clarity, m/z ratios are only given up to m/z 50, although very weak peaks related to more complex hydrocarbons containing up to six carbon atoms are observed (in good agreement with a recent study following an identical experimental protocol (Paardekooper et al., 2014).

The mass spectra of the unprocessed CH_4 ice (dark blue in figure 4.1) depicts low intensity mass peaks above m/z 16 related to light clusters that disappear later on. Figure 4.1 clearly shows a homologous series of straight-chained hydrocarbons, steadily appearing with irradiation time (C_2H_x and C_3H_y, with x = 2, 4, 6 and y = 4, 6, 8). The set of peaks belonging to the homologous series, generally decreases in intensity with increasing

m/z ratios, meaning that the abundances of the photoproducts decrease with molecular complexity. This is consistent with the fact that longer multi-step processes are needed to form more complex species.

In constrast to soft and selective ionisation techniques, 70 eV electron impact sources provide a large number of ions with an extensive fragmentation. Although fragmentation is useful for structure determination, it can also provide mass spectra congested with overlapping fragment peaks and barely visible molecular ion peaks, thus making the interpretation difficult. As a solution and following the quantitative approach used in Paardekooper et al. (2014), each spectrum recorded at a specific irradiation time is regarded as a composite mass spectrum of individual compounds present in the ablated material. For quantification, a fitting procedure is used that needs (i) the different reference mass spectra (Stein, 2014) of CH_4, C_2H_6, C_2H_4, and C_2H_2, and (ii) the corresponding electron impact cross sections at 70 eV (3.524, 6.422, 5.115, and 4.374 $Å^2$, respectively (Kim et al., 2014)) as input, and that provides molar fractions as output. We can therefore determine the temporal decay of CH_4 and the related growth of C_2H_6, C_2H_4, and C_2H_2 as shown in figure 4.2 (full circles).

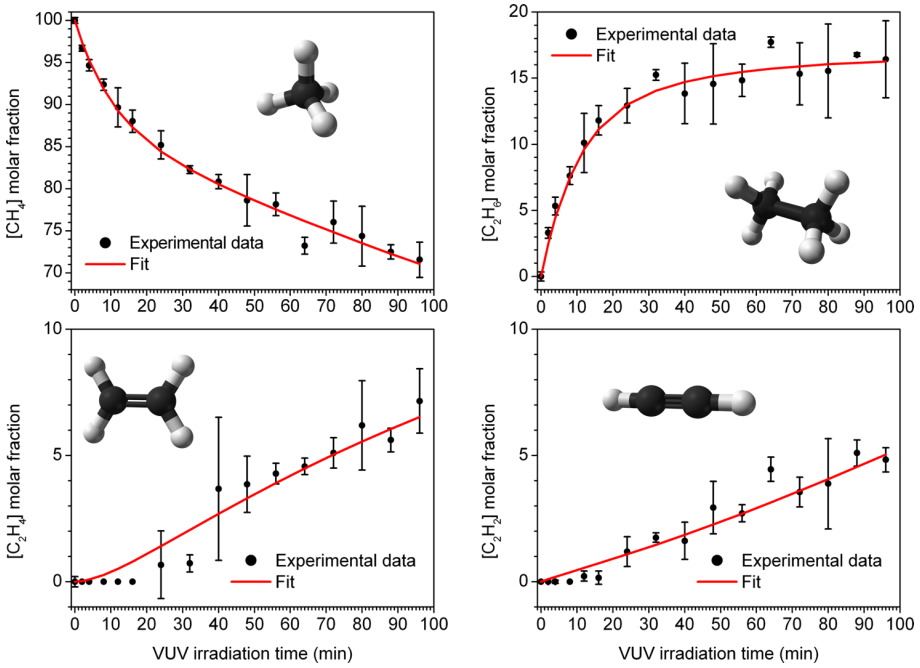

Figure 4.2: Temporal growth and decay of the molar fractions (full circles) of photoproducts and initial material, extracted from the ReTOF mass spectra shown in given in figure 4.1. Fit (in red) of the reduced chemical model (Table 4.1 and Eqs. 6–11) to the molar fractions of methane (*top left*, initial material), ethane (*top right*, photoproduct), ethylene (*bottom left*, photoproduct), and acetylene (*bottom right*, photoproduct). The experimental error bars are representative of the repeatability of the measurements only.

As a check, we extended the set of reference spectra with hydrocarbons containing up to three carbon atoms, thus adding C_3H_8, C_3H_6 and the two C_3H_4 isomers, and we found that these more complex molecules only count for about 4% of the ice mixture at the highest irradiation value (96 min.), meaning that the main photoproducts are – in this study – hydrocarbons with one or two carbon atoms. This will simplify our reaction scheme model

and the total number of parameters to optimise in the next section. Also, a straight exclusion of these larger species does not result in a substantial increase in the uncertainty of the derived parameters. It is important to note at this point that the quantitative approach described above is only used for electron impact mass spectra interpretation by taking into account the fragmentation and that the corresponding outcome is used – in a further step – in a reaction scheme model to understand the actual photochemical processes taking place within the ice.

4.3.1 *Proposed reaction scheme*

We propose a reduced chemical network that is initiated by the methane photodissociation yielding the first generation of photoproducts, i.e., the CH_3, CH_2, and CH radicals, followed by *radical–neutral* and *radical–radical* reactions that form the second generation of photoproducts (e.g., C_2H_6, C_2H_4, and C_2H_2). Then, we allow a limited interplay between each generation of photoproducts, that eventually leads to other hydrocarbons up to two carbon atoms. The reactions considered for the reduced chemical network are given in Table 4.1 and this network comprises a set of 15 distinct reactions with a corresponding R-labeling.

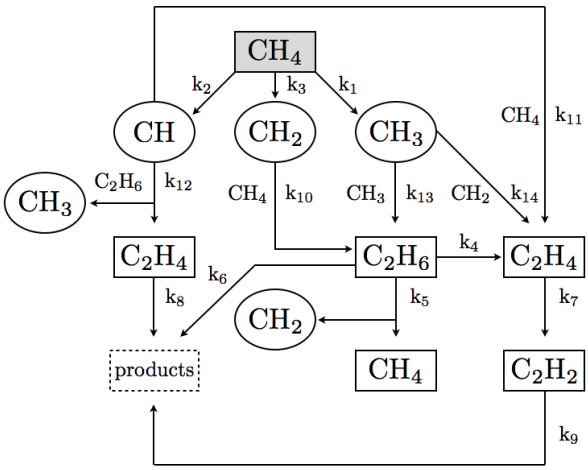

Figure 4.3: Schematic diagram illustrating the reduced reaction network considered in this study. Rectangles indicate stable end-products observable using the LDPI TOF-MS technique, ovals indicate radicals, and the dotted rectangle concerns precursors of hydrocarbons containing more than two carbon atoms.

A schematic diagram is given in figure 4.3 and illustrates the reduced reaction network considered in this study. Note that the model does not take into account tunnelling effects, radical conversions, neither the successive fragmentations of CH_3 leading to CH_2+H and to CH+H radicals; the measured branching ratios are effective values within these settings. Since the *radical–radical* reactions involving the CH_3 and CH_2 radicals (R13-R15) are exothermic and require almost no entrance barrier (Woon, 2002), we assume that they are efficient even at 20 K and occur much faster than the photodissociation pathways that

produce these two radicals (R1 and R3). Thus these two latter routes are assumed to be rate-determining steps. In this way we limit our system to 12 parameters (i.e., reaction rates) instead of 15, initially. The corresponding rate equations (Eqs. 6–11) are listed here in full detail to exclude any ambiguity in the analysis, with the time dependent molar fractions in brackets and the involved reaction numbers in parentheses:

$$\begin{aligned}\frac{d[CH_4]}{dt} = &-2\,k_1\,[CH_4]^2 \quad (R1/R13)\\ &-k_{11}\,[CH_4]\,[CH]-k_2\,[CH_4] \quad (R2/R11)\\ &+k_5\,[C_2H_6] \quad (R5)\\ &-2\,k_3\,[CH_4]^2 \quad (R3/R15)\\ &-k_1\,[CH_4]-k_3\,[CH_4] \quad (R1/R3/R14)\\ &-k_2\,[CH_4] \quad (R2/R12)\\ &-k_3\,[CH_4]-k_{10}\,[CH_4]\,[CH_2] \quad (R3/R10)\end{aligned} \tag{6}$$

Table 4.1: Overview of the reactions involved in this study

Reaction Number	Reaction Type	Rate constant (in s^{-1})
	Photodissociation (first order)	
R1	$CH_4 + h\nu \rightarrow CH_3 + H$	k_1
R2	$CH_4 + h\nu \rightarrow CH + H + H_2$	k_2
R3	$CH_4 + h\nu \rightarrow CH_2$ [a] $+ 2H/H_2$	k_3
R4	$C_2H_6 + h\nu \rightarrow C_2H_4 + 2H/H_2$	k_4
R5	$C_2H_6 + h\nu \rightarrow CH_4 + CH_2$	k_5
R6	$C_2H_6 + h\nu \rightarrow$ products[b]	k_6
R7	$C_2H_4 + h\nu \rightarrow C_2H_2 + 2H/H_2$	k_7
R8	$C_2H_4 + h\nu \rightarrow$ products[c]	k_8
R9	$C_2H_2 + h\nu \rightarrow$ products[d]	k_9
	Neutral–radical (second order)	
R10	$CH_4 + CH_2 \rightarrow CH_3 + CH_3$	k_{10}
R11	$CH_4 + CH \rightarrow C_2H_4 + H$	k_{11}
R12	$C_2H_6 + CH \rightarrow C_2H_4 + CH_3$	k_{12}
	Radical–radical (second order)	Assumptions:
R13	$CH_3 + CH_3 \rightarrow C_2H_6$	$k_{13} \gg k_1$
R14	$CH_3 + CH_2 \rightarrow C_2H_4 + H$	$k_{14} \gg k_1, k_3$
R15	$CH_2 + CH_2 \rightarrow C_2H_2 + 2H/H_2$	$k_{15} \gg k_3$

[a] Singlet and/or triplet state.
[b] C_2H_5+H and/or CH_3+CH_3.
[c] C_2H_3+H.
[d] C_2H+H and/or C_2+H_2.

$$\begin{aligned}\frac{d[C_2H_6]}{dt} = &+ 2\,k_1\,[CH_4]^2 \quad (R1/R13)\\ &- k_5\,[C_2H_6] \quad (R5)\\ &- k_4\,[C_2H_6] \quad (R4)\\ &- k_{12}\,[C_2H_6]\,[CH] \quad (R2/R12)\\ &- k_6\,[C_2H_6] \quad (R6)\\ &+ k_{10}\,[CH_4]\,[CH_2] \quad (R3/R10)\end{aligned} \tag{7}$$

$$\begin{aligned}\frac{d[C_2H_4]}{dt} = &+ k_{11}\,[CH_4]\,[CH] \quad (R2/R11)\\ &+ k_1\,[CH_4] + k_3\,[CH_4] \quad (R1/R3/R14)\\ &+ k_4\,[C_2H_6] \quad (R4)\\ &- k_7\,[C_2H_4] \quad (R7)\\ &- k_8\,[C_2H_4] \quad (R8)\\ &+ k_{12}\,[C_2H_6]\,[CH] \quad (R2/R12)\end{aligned} \tag{8}$$

$$\begin{aligned}\frac{d[C_2H_2]}{dt} = &+ 2\,k_3\,[CH_4]^2 \quad (R3/R15)\\ &+ k_7\,[C_2H_4] \quad (R7)\\ &- k_9\,[C_2H_2] \quad (R9)\end{aligned} \tag{9}$$

$$\begin{aligned}\frac{d[CH_2]}{dt} = &+ k_5\,[C_2H_6] \quad (R5)\\ &+ k_3\,[CH_4] - k_{10}\,[CH_4]\,[CH_2] \quad (R3/R10)\end{aligned} \tag{10}$$

$$\begin{aligned}\frac{d[CH]}{dt} = &- k_{11}\,[CH_4]\,[CH] \quad (R2/R11)\\ &+ k_2\,[CH_4] - k_{12}\,[C_2H_6]\,[CH] \quad (R2/R12)\end{aligned} \tag{11}$$

4.3.2 *Fitting procedure and data treatment*

The system of coupled differential equations is solved numerically by fitting simultaneously the molar fractions of methane $[CH_4]$, ethane $[C_2H_6]$, ethylene $[C_2H_4]$, and acetylene $[C_2H_2]$ at a given irradiation time grid. The methylene radical (CH_2) and methylidyne radical (CH) are intermediate species regarding the *neutral–radical* reactions (R10 – R12). Since we cannot probe their molar fractions as a function of irradiation time, their relative abundances are simply positive variables in the fitting procedure, with the initial conditions $[CH_2]_{t=0} = [CH]_{t=0} = 0\%$. The rate constant optimisation procedure is driven by Matlab 7.9.0 (R2009b) and combines the built-in *ode45* function (ordinary differential equation solver Runge–Kutta 4^{th} and 5^{th} order) with the Nelder-Mead algorithm (Lagarias et al., 1998). The parameter optimisation is proceeded by trying to minimise the squared differences (errors) between the model predictions (y^p) and the experimental values (y):

$$\mathrm{SSE} = \sum_{k=1}^{16}\sum_{l=1}^{4}(y_k - y_k^p)^2, \tag{12}$$

Where k is the number of data points and l corresponds to the number of monitored species. In data fitting, it is usually assumed that the smallest parameter set will provide the most reasonable predictions. The proposed reduced chemical model corresponds to a 12 parameters problem which implies that the function surface has several local solutions. An initial guess of parameters is always required before an optimisation procedure can start. Because the function evaluation (i.e., SSE) strongly depends on the initial set of parameters, the optimisation procedure is repeated many times (e.g., up to 2000 times). This approach is time consuming but creates probability distributions of the estimated parameters, thus providing the statistical analysis tools to (i) estimate the parameters and associated standard errors and (ii) test the linear relationship between each parameter. Before each cycle, an uniformly distributed initial set of 12 rate constants is chosen pseudorandomly from 10^{-1} to 10^{-12} min^{-1}. Each of them can later on vary freely from 0 to 10^{-1} min^{-1} in order to better fit the chemical model to the experimental data. A poor set of starting parameters can lead to a local solution and/or a poor fit, thus giving errors in the rate constants estimation. For this reason, weights (w) are implemented within the different fitting results and they are defined as $1/SSE^2$ so better fits count more than poor ones. The weighted mean (μ_w) and weighted standard deviation (σ_w) are then used to provide an unbiased estimate of both the mean and the standard deviation of the optimised rate constants.

Table 4.2: Effective rate constants and corresponding standard errors of the mean derived from fitting the reduced chemical model (Table 4.1 and Eqs. 6–11) to the experimental data.

Effective Rate Constants (μ_w in s^{-1})		SEM ($\frac{1}{\sqrt{n}} \times \sigma_w$ in s^{-1})
k_5	$= 1.038 \times 10^{-3}$	5×10^{-6}
k_{12}	$= 5.3 \times 10^{-4}$	2×10^{-5}
k_{11}	$= 4.9 \times 10^{-4}$	2×10^{-5}
k_7	$= 1.33 \times 10^{-4}$	3×10^{-6}
k_4	$= 1.115 \times 10^{-4}$	5×10^{-7}
k_9	$= 5.3 \times 10^{-5}$	3×10^{-6}
k_8	$= 2.2 \times 10^{-5}$	2×10^{-6}
k_{10}	$= 7 \times 10^{-6}$	2×10^{-6}
k_6	$= 1.7 \times 10^{-6}$	1×10^{-7}
k_1	$= 1.120 \times 10^{-6}$	3×10^{-9}
k_3	$= 4.26 \times 10^{-8}$	3×10^{-10}
k_2	$= 2.1 \times 10^{-8}$	5×10^{-9}

The weighted mean of each rate constant is given in Table 4.2, together with the standard error of the mean ($SEM = \frac{1}{\sqrt{n}} \times \sigma_w$). The weighted correlation coefficients (rw) are given is Table 4.3 and correspond to real numbers ranging from -1 (anti-correlated) to $+1$ (correlated). The diagonal elements of the correlation matrix are unity by definition. Furthermore, the correlation matrix is a symmetrical matrix so only the lower diagonal is presented. As the rw-values approach zero, the related pair of rate constants is considered either less correlated or uncorrelated. The resulting fits of the reduced chemical model (Eqs. 6–11) to the different molar fraction evolutions are depicted in figure 4.2 and reproduce

Table 4.3: Weighted correlation coefficients (rw) between optimised rates constants ranging from k_1 to k_{12}.

	k_1	k_2	k_3	k_4	k_5	k_6	k_7	k_8	k_9	k_{10}	k_{11}	k_{12}
k_1	1.00	–	–	–	–	–	–	–	–	–	–	–
k_2	-0.06	1.00	–	–	–	–	–	–	–	–	–	–
k_3	0.42	-0.02	1.00	–	–	–	–	–	–	–	–	–
k_4	-0.54	-0.18	-0.92	1.00	–	–	–	–	–	–	–	–
k_5	0.94	-0.03	0.45	-0.52	1.00	–	–	–	–	–	–	–
k_6	-0.34	0.06	-0.23	0.13	-0.33	1.00	–	–	–	–	–	–
k_7	-0.39	0.00	-0.89	0.87	-0.42	0.17	1.00	–	–	–	–	–
k_8	-0.29	0.02	-0.20	0.32	-0.28	0.13	0.19	1.00	–	–	–	–
k_9	-0.29	0.02	-0.54	0.60	-0.30	0.12	0.64	0.10	1.00	–	–	–
k_{10}	-0.41	-0.01	-0.21	0.36	-0.17	0.06	0.20	0.05	0.14	1.00	–	–
k_{11}	0.04	0.01	-0.06	0.05	0.04	-0.02	0.05	0.00	0.03	-0.01	1.00	–
k_{12}	0.04	0.01	-0.04	0.03	0.04	-0.02	0.04	0.01	0.02	0.00	0.16	1.00

the experimental data well, with some deviations for short irradiation times for ethane (C_2H_6) and ethylene (C_2H_4).

4.4 DISCUSSION

We discuss now the results presented above concerning the methane ice photochemistry and kinetic study in the solid phase. The photo-destruction of pure methane leads to the formation of larger photoproducts with numerous unsaturated compounds. After 96 min. of VUV irradiation at 20 K, the composite ice material is mainly formed by CH_4 (70 - 75 %), i.e., CH_4 molecules that have not been consumed or that have been simply reformed, and the rest being photoproducts with up to two carbon atoms. More complex hydrocarbons beyond three C-atoms can be observed but are not taken into account, as discussed earlier. Any quantitative analysis of these hydrocarbons is therefore difficult and provides large uncertainties. However, processes that are diffusion driven like radical-radical reactions involving heavier radicals (e.g., C_2H_5 precursor of C_3- and C_4-hydrocarbons) will be likely enhanced at higher temperatures, thus changing the ice chemistry. The proposed reduced chemical model (Table 4.1 and Eqs. 6–11) includes the three main photodissociation channels of methane and the formation/destruction routes of the three stable photoproducts containing up to two carbon atoms. The proposed model is based on the extensive work performed by the atmospheric chemistry community. We therefore assume that the overall reaction steps collected in the literature from the gas phase studies are also applicable in the solid phase (in contrast to the reaction rate coefficients). We would like to stress that one radical-radical reaction currently listed in the UMIST Database for Astrochemistry (McElroy et al., 2013) was originally included in the model and has been removed. This recombination reaction involves two methyl (CH_3) radicals but in contrast to reaction R13, yields acetylene (C_2H_4) and a molecular hydrogen (H_2):

$$CH_3 + CH_3 \rightarrow C_2H_4 + H_2 \tag{13}$$

By cancelling one by one the different reaction steps in the reduced chemical model, it appears that the presence of this reaction (Eq. 13) never provides a satisfactory conver-

gence criterium in the fitting procedure. Although the molar fractions of acetylene (C_2H_2) were well predicted, the other three molar fractions were largely over- and under-estimated along with the irradiation time, thus leading to a poor fit and finally to the conclusion that this reaction (Eq. 13) likely does not occur in the solid phase.

The photodissociation rates of pure methane ice at 20 K is rather slow with less than 30 % converted in more complex hydrocarbons at the end of 96 min. of photolysis (simulating up to 10^7 years in dense molecular clouds (Prasad & Tarafdar, 1983)). In the reduced chemical model, we assume that R1 and R3 are rate-determining steps. In Table 4.2 we observe that these two photodissociation pathways yielding CH_3 and CH_2 radicals are among the slowest steps in the network ($\leqslant$ 0.1% of the fastest reactions) and therefore determine the rate at which the overall scheme proceeds. This also means that pure methane ices have a remarkable stability under harsh VUV conditions. Previous experimental studies on ices have demonstrated that the photodissociation rates of methane strongly depend on the environment (Cottin et al., 2003). Water-rich porous environments may also affect the diffusion of both neutral and radicals photoproducts (Bossa et al., 2014; Cazaux et al., 2015). Compared to photodissociation rates measured in the gas phase, photodissociation rates in the solid phase are in general substantially lower, most likely because of the fast reverse reactions between the dissociation fragments (Öberg et al., 2010). The reverse reactions R1 and R3 that reform methane and reaction R5 that converts a photoproduct in methane are therefore non negligible in the solid phase. Unsaturated species are less abundant and shielding effects can also play a major role in the chemical evolution and composition of the processed ice. It is for example well known that ethane (C_2H_6) and most higher alkanes are efficiently shielded by methane (CH_4) in the gas phase (Yung & Demore, 1999; Moses et al., 2005), so its destruction is negligible compared to ethylene (C_2H_4) which is less shielded and therefore more destroyed. In this study, we observe that ethane (C_2H_6) is the most abundant photoproduct (Baratta et al., 2002) after ethylene (C_2H_4). This follows the shielding effects observed in the gas phase that seem to apply to the solid state as well.

Following the correlation matrix given in Table 4.3, there are no significant correlations between the optimised parameters k_1, k_2, and k_3, corresponding to the effective rate constants of the different photodissociation channels of methane leading to CH_3, CH, and CH_2 radicals, respectively. We can therefore determine the corresponding branching ratios with good confidence. Table 4.4 lists the calculated branching ratios for the three photodissociation channels of methane in comparison with gas phase data from the literature (Heck et al., 1996; Park et al., 2009; Lodriguito et al., 2009; Gans et al., 2011; Blitz & Seakins, 2012). These results are based on a stable end-products analysis that overcomes the intermediate species detection problem with realistic assumptions. The remaining effective rate constants can be used for any solid state modelling of cold surface irradiation containing methane. Each effective rate constant can be written as $k = \sigma f$, where σ corresponds to the photodissociation cross section for a given reaction (essential for models of interstellar chemistry), and f the given integrated emission flux. It is important to note that strong correlations between a pair of parameters means that both are simultaneously adjusted during the fitting procedure. Therefore, care is needed in their use and interpretation, since these parameters compensate each other (anti-correlated) or vary in about the same proportion (correlated). In this specific case, resulting parameter values and associated errors can be questionable. In our study, only few parameters present significant correlations (k_3/k_4, k_1/k_5, k_3/k_7, and to a lesser extend k_4/k_9 and k_7/k_9), which gives proof of the reliability of the overall network and fitting procedure, but also demonstrates that the parameter estimation remains difficult. The origin of parameter correlations can be diverse and does not necessarily imply the underlying physical or chemical process being studied. For example, a limited set of experimental observations or the fitting process itself

can also induce correlations (Johnson, 2000). Although weighted out, parameters deduced from poor fits still count in the probability distributions of the estimated parameters and may induce correlations. We also observe an intrinsic correlation between k_4 and k_7 which are associated to dehydrogenation processes R4 and R7. These two reactions are linked and yield sequentially ethylene (C_2H_4) and acetylene (C_2H_2) via very similar pathway involving the elimination of a molecular hydrogen (H_2). In addition, both reactions present similar kinetic rates. Therefore, it is not surprising that the corresponding rate constants are correlated: altering either parameter during the fitting procedure induces intrinsically a compensative change in the other.

We conclude now with interpreting the resulting values listed in Table 4.4. Most experimental studies in the gas phase agree that CH radical is the less abundant first generation photoproduct formed during the photolysis of methane (Romanzin et al., 2005; Blitz & Seakins, 2012). We observe the same trend in the solid phase: the CH radical is produced in trace amount (around 2%). The branching ratios are drastically different than those obtained in the gas phase (see also Table 4.4), thus reinforcing the hypothesis that the environment and reverse reactions (unlikely to occur in the gas phase) drive the photoproduct distributions during an irradiation. The primary process yielding the methyl radical (CH_3) is predominant at 20 K, so saturated species and hydrocarbons containing branched alkyl chains are likely expected. Since the reaction requiring the least energy occurs the fastest (Arrhenius law), we assume that the energies required to produce the two other radicals are above the energy required to produce the CH_3 radical (Bennett et al., 2006). This study can help in the identification of hydrocarbons on solar sytem bodies like Saturn's moon Titan that can present pure methane (CH_4) ice in solid aerosols or surface material. However, the pure methane ice studied here cannot be simply extrapolated to environments where ices are likely to be mixed. The branching ratios determined in this work cover the wavelength range of a specific microwave discharge H_2 flow lamp setting. Although pure methane ice presents high absorption close to Lyman-α and very weak absorption from 132 to 165 nm (Wu et al., 2012; Cruz-Diaz et al., 2014), this might not be always the case, especially for photoproducts that absorb at other available wavelengths. Future work should now focus on monochromatic irradiations as well as binary ice mixtures (e.g., N_2:CH_4 or porous H_2O:CH_4).

Table 4.4: Comparison of methane photodissociation pathways in the solid state (this work) and previous gas phase studies. Branching ratios are given in % (adapted from Blitz & Seakins, 2012):

Photolysis pathways:	CH_4 + Ly-α → CH_3 + H	CH_4 + Ly-α → CH_2 + 2H/H_2	CH_4 + Ly-α → CH + H + H_2
This study (solid phase, 20 K)	95±5	4±1	2±1
Gans et al. (2011)[a]	42±5	51±10	7
Lodriguito et al. (2009)[a]	39±3	60±7	15±8
Park et al. (2009)[a]	31±5	69	–
Heck et al. (1996)[a]	66	22	11
Mordaunt et al. (1993)[a]	49	0	51

[a] Gas phase study.

4.5 CONCLUSIONS

The results presented here demonstrate that the LDPI TOF-MS technique can be used to perform a systematic kinetic study on the methane photolysis in the condensed phase at 20 K and provide for the first time effective rate constants and branching ratios for primary processes under VUV light dominated by Lyman-α photons. This work is therefore relevant for modelers in astrochemistry and planetary science. This new experimental approach avoids the problems commonly encountered when using the regular surface science techniques such as limited sensitivity during TPD, infrared band strengths uncertainties, infrared band profile and infrared band overlaps (RAIRS) particularly, in the specific case of complex ices.
The main conclusions of the present work are:

- The photodissociation rates of pure methane ice at 20 K for VUV light dominated by Lyman-α photons are rather slow with less than 30 % converted to stable end-product hydrocarbons containing two carbon atoms (ethane being the most abundant photoproduct after ethylene and acetylene) for a total VUV fluence exposure of $\sim 1 \times 10^{17}$ photons cm^{-2}.

- The rate constants of the different photodissociation channels of methane strongly depend on the environment. The resulting branching ratios derived here for pure methane ice clearly deviate from previous gas phase values.

- Astrochemical models use and often extrapolate gas phase reaction rate coefficients for the solid state. This study shows that this may lead to considerable errors. It also shows that laboratory kinetics studies in the solid phase are now possible and provide for the first time data highly needed in astrochemical models.

BIBLIOGRAPHY

Baratta, G. A., Leto, G., & Palumbo, M. E. 2002, Astron. Astrophys., 384, 343
Bennett, C. J., Jamieson, C. S., Osamura, Y., & Kaiser, R. I. 2006, Astrophys. J., 653, 792
Blitz, M. A. & Seakins, P. W. 2012, Chem. Soc. Rev., 41, 6318
Bossa, J.-B., Borget, F., Duvernay, F., et al. 2012a, Aust. J. Chem., 65
Bossa, J.-B., Isokoski, K., de Valois, M. S., & Linnartz, H. 2012b, Astron. Astrophys., 545, A82
Bossa, J.-B., Isokoski, K., Paardekooper, D. M., et al. 2014, Astron. Astrophys., 561, A136
Brunetto, R., Caniglia, G., Baratta, G. A., & Palumbo, M. E. 2008, Astrophys. J., 686, 1480
Cazaux, S., Bossa, J.-B., Linnartz, H., & Tielens, A. G. G. M. 2015, Astron. Astrophys., 573, A16
Chen, Y.-J., Chuang, K.-J., Muñoz Caro, G. M., et al. 2014, Astrophys. J., 781, 15
Cottin, H., Moore, M. H., & Bénilan, Y. 2003, Astrophys. J., 590, 874
Cruz-Diaz, G. A., Muñoz Caro, G. M., Chen, Y.-J., & Yih, T.-S. 2014, Astron. Astrophys., 562, A120
Dobrijevic, M., Ollivier, J. L., Billebaud, F., Brillet, J., & Parisot, J. P. 2003, Astron. Astrophys., 398, 335
Dohnálek, Z., Kimmel, G. A., Ayotte, P., Smith, R. S., & Kay, B. D. 2003, J. Chem. Phys., 118, 364
El-Adawi, M. K. & Elshehawey, E. F. 1986, J. Appl. Phys., 60, 2250
Focsa, F. & Destombes, J. 2001, Chem. Phys. Lett., 347, 390
Gans, b., Boye-Peronne, S., Broquier, M., et al. 2011, Phys. Chem. Chem. Phys., 13, 8140
Gerakines, P. A., Schutte, W. A., & Ehrenfreund, P. 1996, Astron. Astrophys., 312, 289
Gibb, E. L., Whittet, D. C. B., Boogert, A. C. A., & Tielens, A. G. G. M. 2004, Astrophys. J. Suppl. Ser., 151, 35
Gudipati, M. S. & Yang, R. 2012, Astrophys. J. Lett., 756, L24
Heck, A. J. R., Zare, R. N., & Chandler, D. W. 1996, J. Chem. Phys., 104, 4019
Johnson, M. L. 2000, Numerical Computer Methods, Part C, Vol. 321 (Academic Press), 424–446
Kim, Y.-K., Irikura, K., Rudd, M., et al. 2014, Electron-impact cross sections for Ionization and Excitation
Kim, Y. S. & Kaiser, R. I. 2011, Astrophys. J., 729, 68
Lagarias, J., Reeds, J., Wright, M., & Wright, P. 1998, SIAM. J. Optim., 9, 112
Lee, L. C. & Chiang, C. C. 1983, J. Chem. Phys., 78, 688
Ligterink, N. F. W., Paardekooper, D. M., Chuang, K.-J., et al. 2015, Astron. Astrophys., 584, A56
Lodriguito, M. D., Lendvay, G., & Schatz, G. C. 2009, J. Chem. Phys., 131, 224320
Manion, J. A., Huie, R. E., Levin, R. D., et al. Release 1.6.8, Data version 2013.03, National Institute of Standards and Technology, Gaithersburg, Mary- land, 20899-8320, 2013, http://kinetics.nist.gov/, NIST Chemical Kinetics Database, NIST Standard Reference Database 17, Version 7.0 (Web Version)
McElroy, D., Walsh, C., Markwick, A. J., et al. 2013, Astron. Astrophys., 550, A36
Mispelaer, F., Theulé, P., Aouididi, H., et al. 2013, Astron. Astrophys., 555, A13
Mordaunt, D. H., Lambert, I. R., Morley, G. P., et al. 1993, J. Chem. Phys., 98, 2054
Moses, J. I., Fouchet, T., Bézard, B., et al. 2005, J. Geophys. Res., 110, E08001
Oba, Y., Chigai, T., Osamura, Y., Watanabe, N., & Kouchi, A. 2014, Meteoritics and Planetary Science, 49, 117
Öberg, K. I., Boogert, A. C. A., Pontoppidan, K. M., et al. 2011, Astrophys. J., 740, 109
Öberg, K. I., Bottinelli, S., Jørgensen, J. K., & van Dishoeck, E. F. 2010, Astrophys. J., 716, 825
Öberg, K. I., Fraser, H. J., Boogert, A. C. A., et al. 2007, Astron. Astrophys., 462, 1187
Öberg, K. I., Garrod, R. T., van Dishoeck, E. F., & Linnartz, H. 2009, Astron. Astrophys., 504, 891
Okabe, H. 1978, Photochemistry of small molecules
Paardekooper, D. M., Bossa, J.-B., Isokoski, K., & Linnartz, H. 2014, Rev. Sci. Instrum., 85, 104501
Park, J., Lee, P., Sim, K., Wook Han, J., & Yi, W. 2009, Bull. Korean Chem. Soc., 29, 177
Prasad, S. S. & Tarafdar, S. P. 1983, Astrophys. J., 267, 603
Romanzin, C., Gazeau, M.-C., Bénilan, Y., et al. 2005, Adv. Space Res, 36, 258
Shkrob, I. A., Marin, T. M., Adhikary, A., & Sevilla, M. D. 2011, J. Phys. Chem. C., 115, 3393
Smith, G. P. & Nash, D. 2006, Icarus, 182, 181
Stein, S. 2014, "Mass Spectra" in NIST Chemistry WebBook, NIST Standard Reference Database Number 69, Eds. P.J. Linstrom and W.G. Mallard, National Institute of Standards and Technology, Gaithersburg MD, 20899, http://webbook.nist.gov, (retrieved May 7, 2014).
Theulé, P., Duvernay, F., Danger, G., et al. 2013, Adv. Space Res, 52, 1567
Toriyama, K. & Iwasaki, M. 1979, J. Am. Chem. Soc, 101, 2516
van Dishoeck, E. F. 2014, Farad. Discuss., 168, 9
Wakelam, V., Herbst, E., Loison, J.-C., et al. 2012, Astrophys. J. Suppl. Ser., 199, 21
Wakelam, V., Smith, I. W. M., Herbst, E., et al. 2010, Space Sci. Rev., 156, 13
Wilson, E. H. & Atreya, S. K. 2000, J. Geophys. Res. E, 105, 20263
Woon, D. E. 2002, Astrophys. J. Lett., 571, L177
Wu, Y.-J., Wu, C. Y. R., Chou, S.-L., et al. 2012, Astrophys. J., 746, 175
Yung, Y. L. & Demore, W. B. 1999, Photochemistry in planetary atmospheres, ed. Y. L. Yung & W. B. Demore (Oxford University Press, New York)
Zhitnikov, R. A. & Dmitriev, Y. A. 2002, Astron. Astrophys., 386, 1129